Title

Influence of Atomic Surface Structure on the Activity of Ag for the Electrochemical Reduction of CO 2 to CO

Journal

ACS Catalysis, 9(5)

ISSN

2155-5435

Authors

Clark, EL
Ringe, S
Tang, M
et al.

Publication Date

2019-05-03

DOI

10.1021/acscatal.9b00260

Peer reviewed

ACS Catalysis

Research Article

Cite This: ACS Catal. 2019, 9, 4006−4014

pubs.acs.org/acscatalysis

Influence of Atomic Surface Structure on the Activity of Ag for the Electrochemical Reduction of CO_2 to CO

Ezra L. Clark,[†,‡,⊥] Stefan Ringe,[§,∥,⊥] Michael Tang,[§,∥] Amber Walton,[‡] Christopher Hahn,[§] Thomas F. Jaramillo,[§,∥] Karen Chan,[§] and Alexis T. Bell*[,†,‡]

[†]Joint Center for Artificial Photosynthesis, Lawrence Berkeley National Laboratory, Berkeley, California 94720, United States

[‡]Department of Chemical and Biomolecular Engineering, University of California, Berkeley, California 94720, United States

[§]SUNCAT Center for Interface Science and Catalysis, SLAC National Accelerator Laboratory, Menlo Park, California 94025, United States

[∥]Department of Chemical Engineering, Stanford University, Stanford, California 94305, United States

Supporting Information

ABSTRACT: The present work was undertaken to elucidate the facet-dependent activity of Ag for the electrochemical reduction of CO_2 to CO. To this end, CO_2 reduction was investigated over Ag thin films with (111), (100), and (110) orientations prepared via epitaxial growth on single-crystal Si wafers with the same crystallographic orientations. This preparation technique yielded larger area electrodes than can be achieved using single-crystals, which enabled the electrocatalytic activity of the corresponding Ag surfaces to be quantified in the Tafel regime. The Ag(110) thin films exhibited higher CO evolution activity compared to the Ag(111) and Ag(100) thin films, consistent with previous single-crystal studies. Density functional theory calculations suggest that CO_2 reduction to CO is strongly facet-dependent, and that steps are more active than highly coordinated terraces. This is the result of both a higher binding energy of the key intermediate COOH as well as an enhanced double-layer electric field stabilization over undercoordinated surface atoms located at step edge defects. As a consequence, step edge defects likely dominate the CO_2 reduction activity observed over the Ag(111) and Ag(100) thin films. The higher activity observed over the Ag(110) thin film is then related to the larger density of undercoordinated sites compared to the Ag(111) and Ag(100) thin films. Our conclusion that undercoordinated sites dominate the CO_2 reduction activity observed over close-packed surfaces highlights the need to consider the contribution of such defects in studies of single-crystal electrodes.

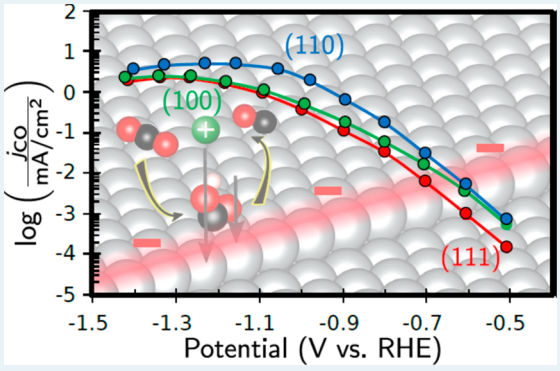

KEYWORDS: *electrocatalysis, carbon dioxide reduction, silver, atomic surface structure, step edge defects*

INTRODUCTION

Understanding the facet-dependence of electrocatalytic conversions is a long-standing topic in electrochemistry and is essential for identifying and optimizing the active sites required to achieve high activity and product selectivity. Work conducted over the past two decades on the electrochemical reduction of CO_2 over Cu,[1−5] Ag,[6,7] Pd,[8] and Rh[9] single-crystal electrodes has suggested that it is possible to distinguish the CO_2 reduction activity of different surface facets. At the same time, theoretical studies have found that CO_2 reduction to CO occurs preferentially at step sites,[10,11] and experiments have revealed that grain-boundary defects are active for CO_2 reduction.[12−14] These facts highlight the importance of understanding the influence of defects on the activity observed over oriented surfaces, since they may contribute in a very significant manner.

Polycrystalline silver (Ag) is one of the only monometallic electrocatalysts capable of achieving CO Faradaic efficiencies (FEs) approaching 100%, with hydrogen (H_2) being the only other product formed.[15−18] The resulting product mixture can then be used to produce hydrocarbons and alcohols by CO hydrogenation.[19−21] Consequently, efforts have been undertaken to improve the CO evolution activity and FE observed over Ag-based electrocatalysts. These studies have revealed that nanostructured Ag exhibits superior CO evolution activity and FE compared to polycrystalline Ag foils over a wide range of potentials.[22−26] What is often not clear is whether the enhanced CO evolution activity observed over nanostructured Ag is due to its higher surface area or to its fundamentally superior intrinsic activity. The difficulty in establishing the primary cause for the superior activity observed over nanostructured Ag is a consequence of the lack of surface-

Received: January 19, 2019
Revised: March 13, 2019
Published: March 19, 2019

DOI: 10.1021/acscatal.9b00260
ACS Catal. 2019, 9, 4006−4014

area normalized activity data.[27] However, in those cases where the intrinsic activity of nanostructured Ag has been measured, its activity has been found to be roughly an order of magnitude higher than that of polycrystalline Ag foil.[22] The superior intrinsic activity observed over nanostructured Ag has been hypothesized to be a consequence of surface defects,[22,25] residual halide promotion,[23] or an elevated local pH.[24]

Theoretical studies of the thermodynamics of CO evolution over different Ag surfaces support the idea that the CO evolution activity of undercoordinated sites is superior to that of basal plane sites.[7,10] However, these studies have not been validated by a concurrent experimental investigation. While CO_2 reduction over Ag single-crystals with different orientations has been reported, the cathode potentials and hence the current densities used were high enough for the mass transfer of CO_2 and ionic species to influence the results.[6] Under such circumstances, changes in the pH and CO_2 concentration near the cathode surface are known to occur, resulting in electrocatalytic activities and selectivities that are not solely reflective of the composition and structure of the electrocatalyst.[6,27,28] Unfortunately, the facet-dependent activity of Ag has not been reported within the Tafel regime due to challenges associated with accurate product quantification over small single-crystal electrodes at low current densities.

The present study was undertaken to gain insights into the facet-dependence of the CO evolution activity of Ag. To this end, we developed a novel method for growing Ag thin films with (111), (100), and (110) orientations by epitaxial growth on single-crystal Si wafers with the same orientations. The large geometric area of these thin film electrodes enabled their electrocatalytic activities to be quantified in the Tafel regime. The Ag(110) thin film exhibited superior intrinsic activity to both the Ag(111) and Ag(100) thin films. Careful DFT analysis that includes the effects of the double-layer electrostatic field shows that defect sites dominate the activity observed over the Ag(111) and Ag(100) thin films, while both the Ag(110) facets and step defects contribute significantly to the activity observed over the Ag(110) thin films. Our analysis highlights the need for careful studies with single-crystals having very low defect densities or the need to block such defect sites, since even a minute fraction of defects is capable of dominating the electrocatalytic activity observed over highly coordinated low-index planes.

EXPERIMENTAL SECTION

Electrode Preparation. Epitaxial Ag thin films were prepared by sputter deposition of Ag (99.999% Kurt J. Lesker) onto polished single-crystal Si wafers (1−10 Ω cm Virginia Semiconductor) with (111), (100), and (110) orientations using an AJA ATC Orion-5 magnetron sputtering system. The native oxide layer on the Si wafers was removed immediately before deposition by submersion in 10 wt % HF. An IR lamp was used to heat the Si wafers to 300 °C prior to and throughout the duration of the deposition. Ag was sputtered onto the etched Si wafers at a rate of 1 Å/s under Ar to obtain a thin film with a thickness of 100 nm.

Electrode Characterization. The crystal structures of the Ag thin films were analyzed with a Rigaku Smartlab X-ray diffractometer (XRD) using Cu Kα radiation (40 kV, 40 mA). Symmetric out-of-plane $\theta/2\theta$ scans were conducted to identify the out-of-plane growth orientation of the Ag crystallites in the thin films. Symmetric in-plane φ scans at Bragg reflections corresponding to both Si and Ag were conducted to determine the orientation of the Ag crystallites with respect to the Si substrate. Symmetric out-of-plane Ω scans were conducted to determine the average degree of misorientation of the Ag crystallites with respect to the surface normal. X-ray pole figures of the Ag thin films were acquired using a PANanalytical X'Pert diffractometer using Cu Kα radiation.

The work functions of the Ag thin films were measured with a Kratos Axis Ultra DLD X-ray photoelectron spectrometer (XPS) using monochromatized Al Kα radiation (15 kV, 15 mA) and an accelerating voltage of 9 V. Ion-scattering spectroscopy (ISS) was also conducted in the same instrument to measure the surface composition of the Ag thin films before and after electrolysis. All spectra were acquired using a He ion beam with an energy of 1 keV. No impurities were detected on the surface of the thin films before or after electrolysis by ISS (see section SI-1).

Electrochemical Characterization. All electrochemical measurements were conducted in a custom gastight electrochemical cell fabricated from a PEEK block.[29] The cell was cleaned prior to each experiment by sonication in 20 wt % nitric acid. An anion-conducting membrane (Selemion AMV AGC Inc.) separated the cathode and anode, which were in a parallel configuration. Each electrode chamber contained a gas dispersion frit to provide ample electrolyte mixing. The geometric surface area of each electrode was 1 cm^2, and the electrolyte volume of each electrode chamber was 1.8 mL. A glassy carbon plate (Type 2 Alfa Aesar) was utilized as the anode. Platinum was not used as the anode due to the possibility of contaminating the cathode.[27,30] The working electrode potential was referenced against a miniature Ag/AgCl electrode (Innovative Instruments Inc.) that was calibrated against a homemade standard hydrogen electrode. Unless stated otherwise the electrolyte was a 0.05 M K_2CO_3 (99.995% Sigma-Aldrich) solution prepared using 18.2 MΩ cm deionized (DI) water with the electrolyte further purified using Chelex 100 (Na form Sigma-Aldrich) to remove trace levels of metal cations.[27,31] Both electrode chambers were sparged with CO_2 (99.999% Praxair Inc.) at a rate of 10 sccm for 30 min prior to and throughout the duration of all electrochemical measurements unless explicitly stated otherwise. Upon saturation with CO_2 the pH of the electrolyte was 6.8, which was maintained throughout the duration of all electrocatalytic measurements. The hydrodynamic boundary layer thickness at the cathode surface was determined to be ∼50 μm by measuring the diffusion limited current of ferricyanide reduction (see section SI-2).

A Biologic VSP-300 potentiostat was utilized to perform all electrochemical measurements. Electrode potentials were recorded versus the reference electrode and converted to the RHE scale. The uncompensated resistance (R_u) of the electrochemical cell was determined by conducting potentiostatic electrochemical impedance spectroscopy (PEIS) with a sinus amplitude of 20 mV and frequencies ranging from 50 Hz to 500 kHz (see section SI-3). For *in situ*, 85% of R_u was compensated for, and the last 15% was postcorrected to arrive at accurate potentials. The redox properties of the Ag thin films were assessed by performing reversible chloride adsorption during cyclic voltammetry from −0.5 to +0.4 V vs SHE at a scan rate of 500 mV/s in 0.01 M KCl saturated with N_2 until a stable voltammogram was obtained, which occurred in approximately 10 cycles.[6] The electrocatalytic activity of each Ag thin film was assessed by conducting chronoamperometry staircases from −0.5 to −1.5 V vs the reversible hydrogen

DOI: 10.1021/acscatal.9b00260
ACS Catal. 2019, 9, 4006−4014

electrode (RHE) with a step size of 100 mV and a step length of 15 min. Each thin film orientation was tested at least three separate times to ensure the statistical relevance of the observed trends. The relative roughness factors of the tested Ag thin films were determined by dividing their double-layer capacitances by the minimum double-layer capacitance measured over the Ag thin films. The double-layer capacitance of each tested Ag thin film was measured by conducting cyclic voltammetry in a potential range where no Faradaic processes occur at a series of increasingly rapid scan rates immediately after the terminal potential of the chronoamperometry staircase was reached (see section SI-4).

Product Analysis. The composition of the electrochemical cell effluent was analyzed using an Agilent 7890B gas chromatograph (GC) equipped with a pulsed-discharge helium ionization detector (PDHID). The effluent was introduced directly into the sample loop of the GC and was sampled at least 10 min after each chronoamperometry potential step. The gaseous constituents of the effluent sample were separated in He (99.9999% Praxair Inc.) using a Hayesep-Q capillary column (Agilent) in series with a packed ShinCarbon ST column (Restek Co.). After opening the gas sampling valve, the column oven of the GC was maintained at 50 °C for 1 min followed by a temperature ramp at 30 °C/min to 250 °C, which was then maintained for the duration of the analysis. The PDHID was calibrated by analyzing a series of NIST-traceable standard gas mixtures (Airgas Inc.) (see section SI-5).

The concentration of liquid-phase products in the electrolyte was determined using a Thermo Scientific UltiMate 3000 liquid chromatograph (HPLC) equipped with a refractive index detector (RID). The electrolyte samples were collected from each electrode chamber after electrolysis stored in a refrigerated autosampler until analyzed. The liquid-phase products contained in a 10 μL aliquot were separated using a series of two Aminex HPX 87-H columns (Bio-Rad Inc.) and a 1 mM sulfuric acid eluent (99.999% Sigma-Aldrich). The column oven was maintained at 60 °C for the duration of the analysis. The signal response of the RID was calibrated by analyzing standard solutions of each product at a concentration of 1, 10, and 50 mM (see section SI-6). The only liquid-phase products observed were trace amounts of formic acid.

Density Functional Theory. Density functional theory calculations of reaction energetics were carried out with a periodic plane-wave implementation and ultrasoft pseudopotentials using QUANTUM ESPRESSO version 5.1[32] interfaced with the Atomistic Simulation Environment (ASE).[33] We applied ultrasoft pseudopotentials and the BEEF-vdW functional, which provides a reasonable description of van der Waals forces while maintaining an accurate prediction of chemisorption energies.[34] Spin-polarized calculations were performed using plane-wave and density cutoffs of 500 and 5000 eV, respectively, as well as a Fermi-level smearing width of 0.1 eV.

In general, adsorption energies were evaluated using four-layer 4 × 4 supercells with all but the top two layers constrained, 20 Å separation of the surface slabs, and [4 × 4 × 1] Monkhorst−Pack k-point grids.[35] For the calculations presented in Figures 5 and 6, 3 × 3 unit cells were used. All structures were relaxed using a BFGS line search algorithm until force components were less than 0.03 eV/Å. A dipole correction was applied to decouple the electrostatic interaction between the periodically repeated slabs. Zero-point energy and finite temperature corrections in the harmonic oscillator approximation were evaluated from the adsorbate vibrations using ASE. We applied a correction of 0.33 eV to the energy of CO_2(g), which was determined from fits to experimental gas-phase reaction energetics.[34] All adsorption energies are available free-of-charge at https://www.catalysis-hub.org/publications/ClarkInfluence2018.

A sawtooth-like external potential (homogeneous electric field) was applied to the relaxed structures along the z-direction (perpendicular to the slabs) with varying field strengths between −0.3 and 0.4 V/Å. Following ref 36, we also applied a dipole correction to decouple the periodic interaction of the slabs in the z-direction. The resulting field-dependent adsorption energies were interpolated with a quadratic polynomial to calculate the dipole moments and polarizabilities. By this procedure, we obtained the analytic field-dependency of all adsorption energies.

RESULTS AND DISCUSSION

Thin Film Deposition. We investigated two approaches for preparing epitaxial Ag thin films on single-crystal Si wafers. The first approach was based on prior studies showing that copper (Cu) thin films can be grown epitaxially on silicon (Si) single-crystal wafers at room temperature.[37−40] Epitaxial growth is possible because Cu diffuses rapidly enough through Si at room temperature to form a copper silicide interlayer during the deposition. This interlayer relaxes the lattice mismatch between Cu and Si, enabling epitaxial growth.[37] The epitaxial growth of silver (Ag) thin films on copper silicide interlayers has also been reported.[41,42] However, epitaxial Ag thin films prepared using this approach exhibited excessive hydrocarbon selectivities uncharacteristic of Ag at potentials cathodic of −1 V vs RHE (see section SI-7). Ion-scattering spectroscopy (ISS) revealed that this is due to the presence of Cu on the surface of these electrodes after CO_2 reduction, which most likely reaches the electrode surface as a consequence of adsorbate induced segregation from the copper silicide interlayer.[43] To avoid this phenomenon, we developed a Cu-free method of epitaxially depositing Ag thin films on single-crystal Si wafers at high temperature. The elevated deposition temperature enables Ag to diffuse rapidly enough through Si to form a silver silicide interlayer during the deposition.

Bulk Crystal Orientation. Symmetric X-ray diffraction (XRD) scans of Ag thin films deposited onto Si(111), Si(100), and Si(110) single-crystal wafers were conducted to determine if the orientation of the Si substrate impacts the out-of-plane growth orientation of the Ag thin films. The only Ag diffraction peaks observed were those corresponding to the orientation of the substrate, indicating that the Ag thin films are textured out-of-plane with orientations matching the substrate (see section SI-8). X-ray pole figures were conducted to determine both the out-of-plane and in-plane orientation of the Ag crystallites in the thin films and validate that they grow epitaxially on the Si substrates. The results are shown in Figure 1. The Ag(200) X-ray pole figure of the Ag thin film deposited onto Si(111) exhibits the 3-fold symmetry characteristic of Ag(111), confirming the epitaxial nature of the thin film with the relationship Si(111)‖Ag{111}. Furthermore, the lack of 6-fold symmetry indicates that the Ag(111) thin films are not twinned.[39] The Ag(111) X-ray pole figure of the Ag thin film deposited onto Si(100) exhibits the 4-fold symmetry characteristic of Ag(100), confirming the epitaxial nature of the thin film

DOI: 10.1021/acscatal.9b00260
ACS Catal. 2019, 9, 4006−4014

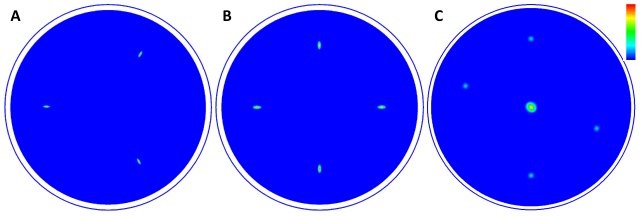

Figure 1. X-ray pole figures of (A) Si(111)‖Ag(111), Ag(200) intensities shown; (B) Si(100)‖Ag(100), Ag(111) intensities shown; and (C) Si(110)‖Ag(110), Ag(022) intensities shown.

with the relationship Si(100)‖Ag{100}. Furthermore, the Ag crystallites in the thin film do not exhibit in-plane rotation relative to the underlying Si substrate, contrary to what has been observed over epitaxially deposited Cu thin films.[38] As a result, the epitaxially deposited Ag thin films exhibit less crystallographic tilt, yielding superior film quality. Finally, the Ag(110) X-ray pole figure of the Ag thin film deposited onto Si(110) exhibits strong intensity parallel to the surface normal, confirming the epitaxial nature of the thin film with the relationship Si(110)‖Ag{110}. Ag(111) and Ag(200) X-ray pole figures of the Ag(110) thin film were also acquired (see section SI-9).

Atomic Surface Structure. Reversible chloride adsorption was conducted over the Ag thin films to confirm their atomic surface structures under near-neutral electrochemical conditions.[6] As shown in Figure 2, distinct redox waves associated

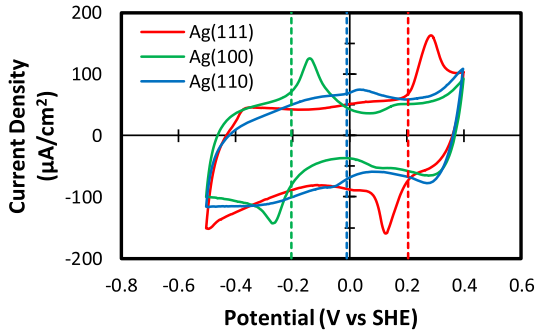

Figure 2. Reversible chloride adsorption over the Ag thin films measured during cyclic voltammetry at 500 mV/s in 0.01 M KCl. The dotted lines correspond to the reversible potentials of chloride adsorption reported over the corresponding Ag single-crystals.[6]

with the reversible adsorption and desorption of chloride anions were observed over each Ag thin film. The consistency of the reversible potentials for chloride adsorption measured over the Ag thin films with those reported over the corresponding Ag single-crystals supports the conclusion that the structure of the surface is consistent with the bulk crystallographic orientation of the Ag thin films. Furthermore, atomic force microscopy (AFM) was conducted over the Ag thin films to visualize their microscopic surface structure (see section SI-10). While Ag(111) and Ag(100) exhibited similar surface roughness, the Ag(110) thin films exhibited more pronounced topological features, in agreement with the higher double-layer capacitance measured over thin films with this crystallographic orientation.

CO_2 Reduction Activity. The CO_2 reduction activity of the Ag(111), Ag(100), and Ag(110) thin films was measured by conducting chronoamperometry staircases from −0.5 to −1.5 V vs RHE in 0.1 M $KHCO_3$, as shown in Figure 3. The observed partial current densities were normalized by the corresponding thin film roughness factors, which were measured by capacitive cycling immediately after the terminal potential of the chronoamperometry staircase was reached. While the roughness factors of the Ag(111) and Ag(100) thin films were found to be roughly equivalent, the Ag(110) thin films exhibited ∼15% higher surface area. The roughness factors and electrocatalytic activities observed over the Ag thin films were found to be highly reproducible from sample to sample, suggesting that the surface structures and defect densities of the thin films are also highly reproducible.

The hydrogen evolution reaction (HER) activity observed over the Ag thin films during CO_2 reduction exhibits three distinct potential regimes. At potentials anodic of −0.7 V vs RHE, the relative HER activities observed over the Ag thin films are consistent with what was observed in the absence of CO_2 (see section SI-11). However, the HER activities are suppressed compared to what would be expected based on an extrapolation of the initial Tafel kinetics at potentials cathodic of −0.7 V vs RHE. Interestingly, prior studies of HER over polycrystalline Ag have also shown that the formation of H_2 is inhibited at potentials cathodic of −0.7 V vs RHE in the presence of CO_2 (see section SI-12).[44] Furthermore, the onset potential for the HER activity suppression agrees well with the onset potential for CO evolution over polycrystalline Ag.[44] Thus, the suppression of HER is likely caused by CO adsorbed on Ag, which has been observed using both Raman and infrared spectroscopies during CO_2 reduction.[45,46] Finally, the HER activity observed over the Ag thin films resumes Tafel behavior at potentials cathodic of −1 V vs RHE. However, the Ag thin films exhibit equivalent HER activities in this potential regime.

The CO evolution activity observed over the Ag thin films exhibits Tafel behavior down to a potential of roughly −1 V vs RHE. Prior investigations of CO_2 reduction over polycrystalline Ag have shown that the CO partial current density is dependent on the hydrodynamics of the electrochemical cell at potentials cathodic of −1 V vs RHE, suggesting that mass transfer limitations cause the CO evolution activity to deviate from Tafel behavior in this potential regime.[27,28,44] Interestingly, the onset of these mass transfer limitations correlates with the recovery of the Tafel behavior of HER observed at potentials cathodic of −1 V vs RHE. This observation provides further support for the hypothesis that the suppression of HER is caused by the adsorption of CO on the Ag surface. Prior to the onset of mass transfer limitations, the intrinsic CO evolution activities observed over the Ag(111) and Ag(100) thin films are approximately equivalent. However, the Ag(110) thin films exhibit superior intrinsic activity to both the Ag(111) and Ag(100) thin films by a factor of ∼5 at −1 V vs RHE. As shown in section SI-13, the relative intrinsic CO evolution activities observed over the Ag thin films are in agreement with what has been observed over Ag(111), Ag(100), and Ag(110) single-crystals.[6] We note, however, these prior activity measurements were conducted at potentials where mass transfer effects begin to be significant and did not span a wide enough potential range for accurate and intrinsic Tafel slopes to be determined.

Theoretical Insights: Structural Sensitivity and Local Field Effects. Recent theoretical studies have concluded that the reduction of CO_2 to CO proceeds via the following elementary steps:[7,10,47,48]

DOI: 10.1021/acscatal.9b00260
ACS Catal. 2019, 9, 4006−4014

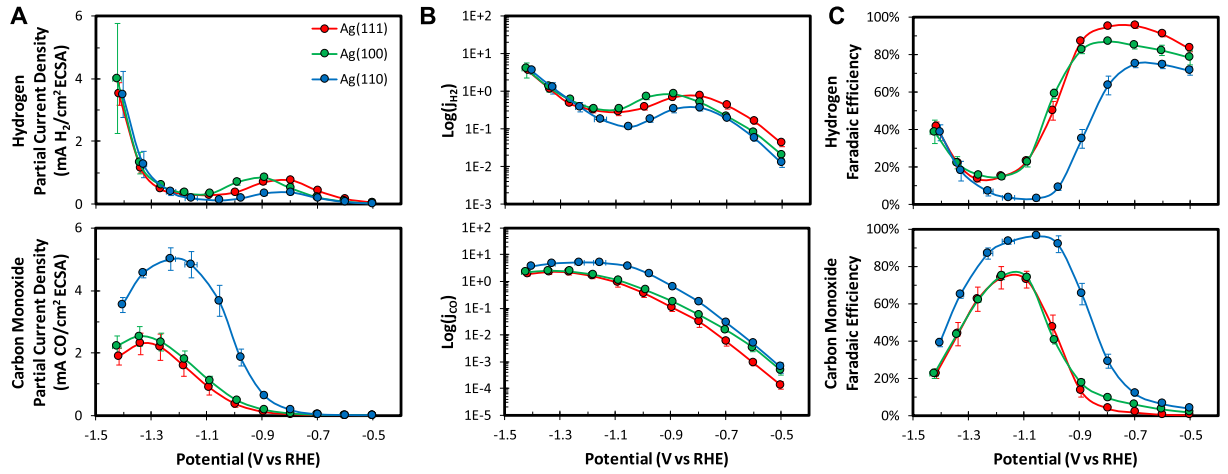

Figure 3. CO_2 reduction activity observed over the Ag(111), Ag(100), and Ag(110) thin films vs applied potential. Partial current densities for H_2 and CO on (A) linear scale and (B) log scale. (C) H_2 and CO Faradaic efficiencies.

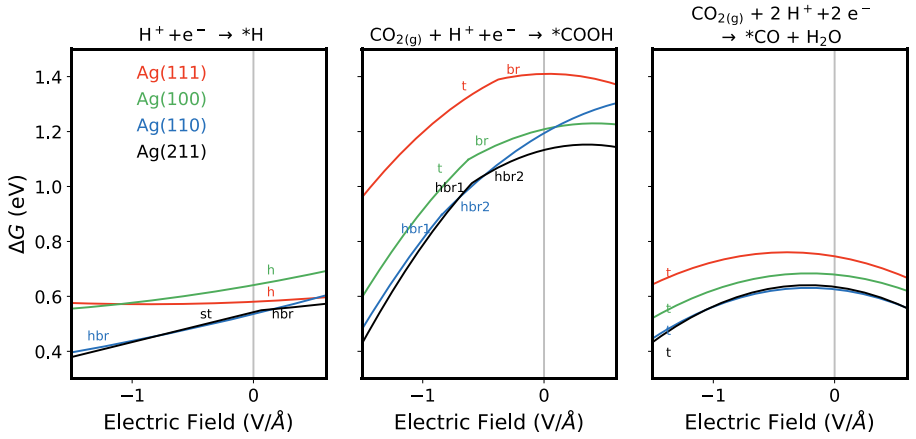

Figure 4. Homogeneous electric-field-dependent binding free energies of reaction intermediates over Ag(111), Ag(100), Ag(110), and Ag(211) at 0 V vs RHE as calculated by applying a sawtooth potential. The solid lines represent a parabolic extrapolation of the calculated data points. Only the most stable adsorption configurations are depicted. Kinks in the solid lines indicate a change in the most stable adsorption site. The adsorption sites are t = top, st = top of the step, h = hollow, br = bridge, and hbr = high bridge.

(1) $CO_2(g) + * + H^+ + e^- \rightarrow *COOH$

(2) $*COOH + H^+ + e^- \rightarrow *CO + H_2O$

(3) $*CO \rightarrow CO(g) + *$

where * refers to an unoccupied site on the catalyst surface and *X (where X = H, COOH, and CO) refers to X adsorbed on the catalyst surface. Proton and electron free energies are treated via the computational hydrogen electrode.[49] Since reaction 1 is the last to become exergonic as the applied potential is made more cathodic, this suggests that it is the rate-determining step of the reaction.[7,10,47,48] However, we note that there is still a debate in the literature about the rate-determining step of CO evolution over Ag and Au electrocatalysts, with some arguing that the adsorption of CO_2 with simultaneous electron transfer is the rate-determining step over Ag[50] and Au surfaces.[51,52] Although various studies on the kinetic isotope effect (KIE) or pH-dependence suggest that this step is the rate-determining step,[51] more recent investigations raised doubt in these conclusions and instead concluded that the reduction of $*CO_2$ to *COOH is the rate-determining step.[52] Assuming that $*CO_2$ and *COOH show similar binding energy trends among different surface facets, the consideration of *COOH as the key intermediate should in both cases be valid for the discussion here. However, future studies should investigate the importance of the first adsorption step in the reaction mechanism to validate this assumption. Previous studies have suggested that the COOH binding energy is highly dependent on the atomic surface structure of the electrocatalyst,[10] with stepped facets generally binding COOH more strongly over all transition metals (see section SI-14). In contrast, the H binding energy is largely structure-insensitive. Since the H binding energy is a good descriptor of HER activity,[53] the intrinsic HER activity of Ag is expected to be largely independent of the atomic surface structure.

Prior work has also shown that local electric fields generated by the presence of excess cations in the Helmholtz plane at potentials cathodic of the potential of zero charge (PZC) can significantly stabilize polarizable reaction intermediates.[4,54] The influence of the electric field strength on the stability of the adsorbed intermediates participating in reactions 1−3 was calculated for different Ag surfaces. As seen in Figure 4, the degree of stabilization for a given species depends on its identity, binding site and configuration, as well as the atomic surface structure and the magnitude of the electric field. Details of these calculations are given in the Supporting Information

DOI: 10.1021/acscatal.9b00260
ACS Catal. 2019, 9, 4006−4014

(see section SI-15). In general, the degree of the electric field stabilization increases with the polarizability and dipole moment of the species in question. As a result, the electric field does not significantly impact the adsorption energy of *H since it is not polarizable and does not possess a significant dipole moment. Thus, the HER activity should be relatively insensitive to the local electric field strength. In contrast, the electric field significantly stabilizes *COOH because it has a large polarizability and dipole moment. The stabilization of *COOH on stepped facets was investigated further using prototypical step models for the (111) and (100) surface facets with different step densities. As shown in Figure 5, the stability

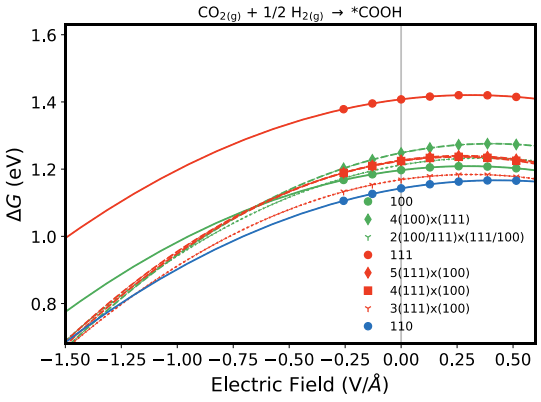

Figure 5. Homogeneous electric-field-dependent binding free energies of *COOH over various Ag facets at 0 V vs RHE as calculated by applying a sawtooth potential. Only the most stable configuration of *COOH at zero field has been considered. Stepped surface facets have been colored according to the prevalent terrace. The step densities increase from solid to dashed to dotted lines.

of *COOH on the (111) facet is enhanced as the step density increases at zero electric field. In contrast, the stability of *COOH on the (100) facet seems to be reduced as the step density increases. Notably, under the influence of negative electric fields, all steps show a similar *COOH binding strength, which is always stronger than the nonstepped terrace.

To investigate the impact of the local electric field on the thermodynamics of CO evolution, we established a link between the electrode potential and the local electric field strength by means of a Poisson–Boltzmann model. The presence of the Helmholtz layer was included by implementing Robin boundary conditions[55] at the electrode surface utilizing the experimentally determined Helmholtz capacitance of 20 μF/cm^2, which is valid for potentials sufficiently negative of the PZC (for details, see section SI-16).[56] In contrast to more advanced models of the double layer, this strategy provides an estimate of the Helmholtz layer field at a certain applied potential by means of a single adjustable parameter, the Helmholtz dielectric permittivity, which we set to 2 according to recent experimental results.[57] The difference in local field magnitude among the Ag facets is then determined based on the PZCs of the respective surfaces. The experimentally measured work functions of the Ag thin films decrease systematically with surface atom density, in agreement with what has been observed over the corresponding Ag single-crystals (see section SI-17).[58] As the work function decreases, the potential of zero charge shifts to more cathodic potentials, as shown in Table S2.[59,60]

The influences of the local electric fields on the reaction thermodynamics are shown in Figure 6. Comparison of the left

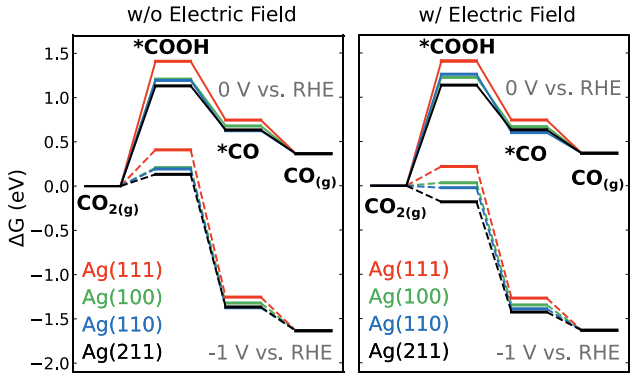

Figure 6. Free energy diagrams for CO_2 reduction to CO over Ag(111), Ag(100), Ag(110), and Ag(211) at 0 V and −1 V vs RHE calculated using the computational hydrogen electrode model. The free energy diagrams in the right panel are corrected by a homogeneous electric field calculated using a mean-field model with a Helmholtz capacitance of 20 μF/cm^2 and a dielectric permittivity of 2. Field-dependencies of the free energies were obtained by applying a sawtooth potential of variable magnitude.

and right panels demonstrates that the inclusion of the mean electrostatic field predominately lowers the free energies for reaction 1 and that this effect is most pronounced for undercoordinated surfaces (i.e., Ag(110) and Ag(211)) at an applied potential of −1 V vs RHE. Thus, the inclusion of field effects further improves the reaction thermodynamics over surfaces with undercoordinated atoms.

Influence of Film Defects on Observed Activity Trends. Step edge defects have been observed at the surface of epitaxial thin films prepared using a similar synthesis protocol.[46] The significantly larger driving force for CO_2 reduction to CO on steps sites, in particular relative to the (111) surface facet, suggests that step edge defects in the epitaxial Ag thin films could contribute disproportionately to the observed activity of (111) and (100) oriented films. The extent to which step edge defects contribute to the electrocatalytic activities observed over the Ag thin films is a function of their abundance and activity relative to terrace sites. Figure 7 presents the results of a simple analysis (see section SI-18) illustrating the contribution of defect sites to the observed activity as a function of their abundance and activity relative to terrace sites. A defect density of 1% is generally enough to dominate the observed activity if their kinetic

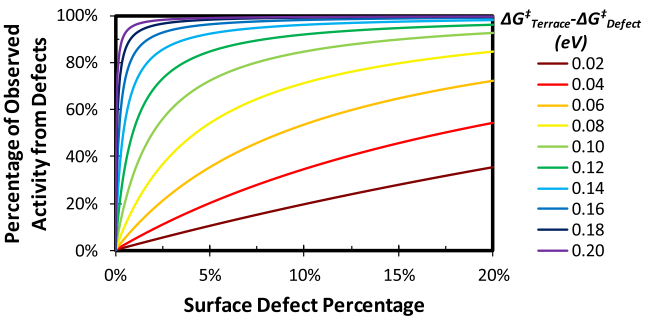

Figure 7. Calculated contribution of defects to the observed activity based on their abundance and activity relative to terrace sites.

DOI: 10.1021/acscatal.9b00260
ACS Catal. 2019, 9, 4006−4014

barriers are only 150 meV lower than that of the majority site. An estimate of the activation barrier difference can be made by taking the Ag(211) surface to be representative of a step edge defect and considering activation barriers for CO evolution to scale linearly with the relative stability of *COOH. Following this approach, a defect density of 1% would totally dominate the activity observed over the Ag(111) thin film. Considering the stabilizing effect of steps shown in Figure 5, we also expect step edge defects to dominate the activity observed over the Ag(100) thin films. In contrast, the COOH binding energy of the (110) surface facet is already steplike and comparable to the (111) and (100) step activity, as shown in Figure 5. Thus, the higher activity observed over the (110) thin films relative to the (111) and (100) thin films could be attributable to an increase in the density of undercoordinated active sites. Since single-crystals typically exhibit a defect density of roughly 1% (based on a typical miscut of 0.5°),[61] a method to titrate these highly active defect sites by selectively blocking them is needed to measure the intrinsic electrocatalytic activity of low-index terraces accurately.[62]

Influence of Local Field Variations. The analysis up to this point applies a mean field approach, which does not consider variations in the local electric field distribution on an atomistic scale. As shown in ref 63, regions of high surface curvature tend to localize surface charge and interfacial electric fields. To investigate the dependence of the local electric field distribution on the atomic surface structure, we applied a linearized Poisson−Boltzmann model of the electrolyte in conjunction with *ab initio* simulations of the various facets. Table S2 shows that the undercoordinated surface generally exhibits significantly larger charge densities, which should give rise to stronger local electric fields (see section SI-19). These local variations in the electric field strength would lead to an enhancement of the activity of undercoordinated sites relative to fully coordinated surfaces. These effects motivate studies of the dependence of the local field distribution on the morphology and atomic surface structure of the electrocatalyst.

CONCLUSIONS

We have developed a novel method for growing epitaxial Ag thin films with (111), (100), and (110) orientations. These large area thin film electrodes enabled the electrocatalytic activities of Ag(111), Ag(100), and Ag(110) to be quantified in the Tafel regime, unlike previous single-crystal studies. The electrochemical reduction of CO_2 to CO over the Ag(110) thin film exhibits superior activity compared to either the Ag(111) or Ag(100) thin films, consistent with previous single-crystal studies. Theoretical analysis indicates that the dependence of the CO_2 reduction activity on atomic surface structure can be attributed to both a general binding preference and an enhanced electric field stabilization of polarizable CO_2 reduction intermediates on undercoordinated surface atoms. Our theoretical analysis indicates that step edge defects exhibit much higher activities than either Ag(111) or Ag(100) surface sites and slightly higher activities than Ag(110) surface sites. Therefore, the higher activity observed over the Ag(110) thin films compared to the Ag(111) and Ag(100) thin films is likely the result of a higher density of undercoordinated active sites. Finally, the results of our theoretical analysis demonstrate that the presence of step edge defects can complicate the quantification of the intrinsic electrocatalytic activity of basal plane sites with relatively low activity. This observation highlights the importance of considering the contributions of defects to the observed CO_2 reduction activity of electrocatalysts. Moreover, it indicates that, to measure the intrinsic activity of low-index facets of single-crystals, such crystals must have very low defect densities, and/or the defect sites need to be poisoned to inactivate them.

ASSOCIATED CONTENT

Supporting Information

The Supporting Information is available free of charge on the ACS Publications website at DOI: 10.1021/acscatal.9b00260.

Validation of surface purity, quantification of the hydrodynamic boundary layer thickness, potentiostatic electrochemical impedance spectroscopy, electrochemically active surface area, gas chromatography, high performance liquid chromatography, comparison of epitaxial growth techniques, out-of-plane and in-plane X-ray diffraction, extended X-ray pole figures, hydrogen evolution, impact of CO_2 on hydrogen evolution, electric-field-dependent binding free energies, work function measurements, calculation of the contribution of defects to the observed activity, surface atom charge calculations, estimation of the potential-field relationship, scaling plots, and defect step models (PDF)

AUTHOR INFORMATION

Corresponding Author

*E-mail: alexbell@berkeley.edu.

ORCID

Christopher Hahn: 0000-0002-2772-6341
Thomas F. Jaramillo: 0000-0001-9900-0622
Karen Chan: 0000-0002-6897-1108
Alexis T. Bell: 0000-0002-5738-4645

Author Contributions

⊥E.L.C. and S.R. contributed equally.

Notes

The authors declare no competing financial interest.

ACKNOWLEDGMENTS

This material is based upon work performed by the Joint Center for Artificial Photosynthesis, a DOE Energy Innovation Hub, supported through the Office of Science of the U.S. Department of Energy under Award DE-SC0004993. This research used resources of the National Energy Research Supercomputer Center, a DOE Office of Science User Facility supported by the Office of Science of the U.S. Department of Energy under Contract No. DE-AC02-05CH11231. E.L.C. was supported by the National Science Foundation (NSF). The authors would also like to thank Dr. Johanna Eichhorn for conducting the atomic force microscopy of the epitaxial Ag thin films.

REFERENCES

(1) Hori, Y.; Takahashi, I.; Koga, O.; Hoshi, N. Electrochemical Reduction of Carbon Dioxide at Various Series of Copper Single Crystal Electrodes. *J. Mol. Catal. A: Chem.* **2003**, *199*, 39−47.

(2) Huang, Y.; Handoko, A. D.; Hirunsit, P.; Yeo, B. S. Electrochemical Reduction of CO2 Using Copper Single-Crystal Surfaces: Effects of CO* Coverage on the Selective Formation of Ethylene. *ACS Catal.* **2017**, *7*, 1749−1756.

(3) Schouten, K. J. P.; Qin, Z.; Pérez Gallent, E.; Koper, M. T. M. Two Pathways for the Formation of Ethylene in CO Reduction on

DOI: 10.1021/acscatal.9b00260
ACS Catal. 2019, 9, 4006−4014

Single-Crystal Copper Electrodes. *J. Am. Chem. Soc.* **2012**, *134*, 9864−9867.
(4) Resasco, J.; Chen, L. D.; Clark, E.; Tsai, C.; Hahn, C.; Jaramillo, T. F.; Chan, K.; Bell, A. T. Promoter Effects of Alkali Metal Cations on the Electrochemical Reduction of Carbon Dioxide. *J. Am. Chem. Soc.* **2017**, *139*, 11277−11287.
(5) Schouten, K. J. P.; Pérez Gallent, E.; Koper, M. T. M. Structure Sensitivity of the Electrochemical Reduction of Carbon Monoxide on Copper Single Crystals. *ACS Catal.* **2013**, *3*, 1292−1295.
(6) Hoshi, N.; Kato, M.; Hori, Y. Electrochemical Reduction of CO2 on Single Crystal Electrodes of Silver Ag(111), Ag(100), and Ag(110). *J. Electroanal. Chem.* **1997**, *440* (1−2), 283−286.
(7) Rosen, J.; Hutchings, G. S.; Lu, Q.; Rivera, S.; Zhou, Y.; Vlachos, D. G.; Jiao, F. Mechanistic Insights into the Electrochemical Reduction of CO2 to CO on Nanostructured Ag Surfaces. *ACS Catal.* **2015**, *5*, 4293−4299.
(8) Hoshi, N.; Noma, M.; Suzuki, T.; Hori, Y. Structural Effect on the Rate of CO2 Reduction on Single Crystal Electrodes of Palladium. *J. Electroanal. Chem.* **1997**, *421*, 15−18.
(9) Hoshi, N.; Ito, H.; Suzuki, T.; Hori, Y. CO2 Reduction on Rh Single Crystal Electrodes and the Structural Effect. *J. Electroanal. Chem.* **1995**, *395*, 309−312.
(10) Shi, C.; Hansen, H. A.; Lausche, A. C.; Nørskov, J. K. Trends in Electrochemical CO2 Reduction Activity for Open and Close-Packed Metal Surfaces. *Phys. Chem. Chem. Phys.* **2014**, *16* (10), 4720.
(11) Durand, W. J.; Peterson, A. A.; Studt, F.; Abild-Pedersen, F.; Nørskov, J. K. Structure Effects on the Energetics of the Electrochemical Reduction of CO2 by Copper Surfaces. *Surf. Sci.* **2011**, *605*, 1354−1359.
(12) Feng, X.; Jiang, K.; Fan, S.; Kanan, M. W. Grain-Boundary-Dependent CO2 Electroreduction Activity. *J. Am. Chem. Soc.* **2015**, *137*, 4606−4609.
(13) Kim, K.-S.; Kim, W. J.; Lim, H.-K.; Lee, E. K.; Kim, H. Tuned Chemical Bonding Ability of Au at Grain Boundaries for Enhanced Electrochemical CO2 Reduction. *ACS Catal.* **2016**, *6*, 4443−4448.
(14) Mariano, R. G.; McKelvey, K.; White, H. S.; Kanan, M. W. Selective Increase in CO2 Electroreduction Activity at Grain-Boundary Surface Terminations. *Science (Washington, DC, U. S.)* **2017**, *358*, 1187−1192.
(15) Hori, Y.; Kikuchi, K.; Suzuki, S. Production of CO and CH4 in Electrochemical Reduction of CO2 at Metal Electrodes in Aqueous Hydrogencarbonate Solution. *Chem. Lett.* **1985**, *14*, 1695−1698.
(16) Noda, H.; Ikeda, S.; Oda, Y.; Imai, K.; Maeda, M.; Ito, K. Electrochemical Reduction of Carbon Dioxide at Various Metal Electodes in Aqueous Potassium Hydrogen Carbonate Solution. *Bull. Chem. Soc. Jpn.* **1990**, *63*, 2459−2462.
(17) Hori, Y.; Wakebe, H.; Tsukamoto, T.; Koga, O. Electrocatalytic Process of CO Selectivity in Electrochemical Reduction of CO2 at Metal Electrodes in Aqueous Media. *Electrochim. Acta* **1994**, *39*, 1833−1839.
(18) Hatsukade, T.; Kuhl, K. P.; Cave, E. R.; Abram, D. N.; Jaramillo, T. F. Insights into the Electrocatalytic Reduction of CO2 on Metallic Silver Surfaces. *Phys. Chem. Chem. Phys.* **2014**, *16*, 13814−13819.
(19) Jitaru, M.; Lowy, D. A.; Toma, M.; Toma, B. C.; Oniciu, L. Electrochemical Reduction of Carbon Dioxide on Flat Metallic Cathodes. *J. Appl. Electrochem.* **1997**, *27*, 875−889.
(20) Gattrell, M.; Gupta, N.; Co, A. A Review of the Aqueous Electrochemical Reduction of CO2 to Hydrocarbons at Copper. *J. Electroanal. Chem.* **2006**, *594*, 1−19.
(21) Hori, Y. Electrochemical CO2 Reduction on Metal Electrodes. In *Modern Aspects of Electrochemistry*; Vayenas, C. G., White, R. E., Gamboa-Aldeco, M. E., Eds.; Springer: New York, 2008; pp 89−189.
(22) Lu, Q.; Rosen, J.; Zhou, Y.; Hutchings, G. S.; Kimmel, Y. C.; Chen, J. G.; Jiao, F. A Selective and Efficient Electrocatalyst for Carbon Dioxide Reduction. *Nat. Commun.* **2014**, *5*, 1−6.
(23) Hsieh, Y.-C.; Senanayake, S. D.; Zhang, Y.; Xu, W.; Polyansky, D. E. Effect of Chloride Anions on the Synthesis and Enhanced Catalytic Activity of Silver Nanocoral Electrodes for CO 2 Electroreduction. *ACS Catal.* **2015**, *5*, 5349−5356.
(24) Ma, M.; Trześniewski, B. J.; Xie, J.; Smith, W. A. Selective and Efficient Reduction of Carbon Dioxide to Carbon Monoxide on Oxide-Derived Nanostructured Silver Electrocatalysts. *Angew. Chem., Int. Ed.* **2016**, *55*, 9748−9752.
(25) Mistry, H.; Choi, Y. W.; Bagger, A.; Scholten, F.; Bonifacio, C. S.; Sinev, I.; Divins, N. J.; Zegkinoglou, I.; Jeon, H. S.; Kisslinger, K.; Stach, E. A.; Yang, J. C.; Rossmeisl, J.; Roldan Cuenya, B. Enhanced Carbon Dioxide Electroreduction to Carbon Monoxide over Defect-Rich Plasma-Activated Silver Catalysts. *Angew. Chem., Int. Ed.* **2017**, *56*, 11394−11398.
(26) Peng, X.; Karakalos, S. G.; Mustain, W. E. Preferentially Oriented Ag Nanocrystals with Extremely High Activity and Faradaic Efficiency for CO2 Electrochemical Reduction to CO. *ACS Appl. Mater. Interfaces* **2018**, *10*, 1734−1742.
(27) Clark, E. L.; Resasco, J.; Landers, A.; Lin, J.; Chung, L.-T.; Walton, A.; Hahn, C.; Jaramillo, T. F.; Bell, A. T. Data Acquisition Protocols and Reporting Standards for Studies of the Electrochemical Reduction of Carbon Dioxide. *ACS Catal.* **2018**, *8*, 6560−6570.
(28) Singh, M. R.; Clark, E. L.; Bell, A. T. Effects of Electrolyte, Catalyst, and Membrane Composition and Operating Conditions on the Performance of Solar-Driven Electrochemical Reduction of Carbon Dioxide. *Phys. Chem. Chem. Phys.* **2015**, *17* (29), 18924−18936.
(29) Lobaccaro, P.; Singh, M. R.; Clark, E. L.; Kwon, Y.; Bell, A. T.; Ager, J. W. Effects of Temperature and Gas-Liquid Mass Transfer on the Operation of Small Electrochemical Cells for the Quantitative Evaluation of CO2 Reduction Electrocatalysts. *Phys. Chem. Chem. Phys.* **2016**, *18*, 26777−26785.
(30) Dunwell, M.; Lu, Q.; Heyes, J. M.; Rosen, J.; Chen, J. G.; Yan, Y.; Jiao, F.; Xu, B. The Central Role of Bicarbonate in the Electrochemical Reduction of Carbon Dioxide on Gold. *J. Am. Chem. Soc.* **2017**, *139*, 3774−3783.
(31) Wuttig, A.; Surendranath, Y. Impurity Ion Complexation Enhances Carbon Dioxide Reduction Catalysis. *ACS Catal.* **2015**, *5*, 4479−4484.
(32) Giannozzi, P.; Baroni, S.; Bonini, N.; Calandra, M.; Car, R.; Cavazzoni, C.; Ceresoli, D.; Chiarotti, G. L.; Cococcioni, M.; Dabo, I.; Corso, A. D.; de Gironcoli, S.; Fabris, S.; Fratesi, G.; Gebauer, R.; Gerstmann, U.; Gougoussis, C.; Kokalj, A.; Lazzeri, M.; Martin-Samos, L.; Marzari, N.; Mauri, F.; Mazzarello, R.; Paolini, S.; Pasquarello, A.; Paulatto, L.; Sbraccia, C.; Scandolo, S.; Sclauzero, G.; Seitsonen, A. P.; Smogunov, A.; Umari, P.; Wentzcovitch, R. M. QUANTUM ESPRESSO: A Modular and Open-Source Software Project for Quantum Simulations of Materials. *J. Phys.: Condens. Matter* **2009**, *21*, 395502.
(33) Hjorth Larsen, A.; Jørgen Mortensen, J.; Blomqvist, J.; Castelli, I. E.; Christensen, R.; Dułak, M.; Friis, J.; Groves, M. N.; Hammer, B.; Hargus, C.; Hermes, E. D.; Jennings, P. C.; Bjerre Jensen, P.; Kermode, J.; Kitchin, J. R.; Leonhard Kolsbjerg, E.; Kubal, J.; Kaasbjerg, K.; Lysgaard, S.; Bergmann Maronsson, J.; Maxson, T.; Olsen, T.; Pastewka, L.; Peterson, A.; Rostgaard, C.; Schiøtz, J.; Schütt, O.; Strange, M.; Thygesen, K. S.; Vegge, T.; Vilhelmsen, L.; Walter, M.; Zeng, Z.; Jacobsen, K. W. The Atomic Simulation Environment—a Python Library for Working with Atoms. *J. Phys.: Condens. Matter* **2017**, *29*, 273002.
(34) Studt, F.; Abild-Pedersen, F.; Varley, J. B.; Nørskov, J. K. CO and CO2 Hydrogenation to Methanol Calculated Using the BEEF-VdW Functional. *Catal. Lett.* **2013**, *143*, 71−73.
(35) Monkhorst, H. J.; Pack, J. D. Special Points for Brillouin-Zone Integrations. *Phys. Rev. B Condens. Matter* **1976**, *13*, 5188−5192.
(36) Meyer, B.; Vanderbilt, D. Ab Initio Study of BaTiO3 and PbTiO3 Surfaces in External Electric Fields. *Phys. Rev. B: Condens. Matter Mater. Phys.* **2001**, *63*, 205426.
(37) Chang, C. A. Formation of Copper Silicides from Cu(100)/Si(100) and Cu(111)/Si(111) Structures. *J. Appl. Phys.* **1990**, *67*, 566−569.

DOI: 10.1021/acscatal.9b00260
ACS Catal. 2019, 9, 4006−4014

(38) Jiang, H.; Klemmer, T. J.; Barnard, J. A.; Payzant, E. A. Epitaxial Growth of Cu on Si by Magnetron Sputtering. *J. Vac. Sci. Technol., A* **1998**, *16*, 3376−3383.
(39) Jiang, H.; Klemmer, T. J.; Barnard, J. A.; Doyle, W. D.; Payzant, E. A. Epitaxial Growth of Cu(111) Films on Si(110) by Magnetron Sputtering: Orientation and Twin Growth. *Thin Solid Films* **1998**, *315*, 13−16.
(40) Krastev, E. T.; Voice, L. D.; Tobin, R. G. Surface Morphology and Electric Conductivity of Epitaxial Cu(100) Films Grown on H-Terminated Si(100). *J. Appl. Phys.* **1996**, *79*, 6865−6871.
(41) Pedersen, K.; Kristensen, T. B.; Pederser, T. G.; Morgen, P.; Li, Z.; Hoffman, S. V. Optimum Cu Buffer Layer Thickness for Growth of Metal Overlayers on Si (111). *Phys. Rev. B: Condens. Matter Mater. Phys.* **2002**, *66*, 1−4.
(42) Pedersen, K.; Morgen, P.; Petersen, T. G.; Li, Z.; Hoffmann, S. V. Epitaxial Growth of Thin Ag and Au Films on Si(111) Using Thin Copper Silicide Buffer Layers. *J. Vac. Sci. Technol., A* **2003**, *21*, 1431−1435.
(43) Clark, E. L.; Hahn, C.; Jaramillo, T. F.; Bell, A. T. Electrochemical CO2 Reduction over Compressively Strained CuAg Surface Alloys with Enhanced Multi-Carbon Oxygenate Selectivity. *J. Am. Chem. Soc.* **2017**, *139* (44), 15848−15857.
(44) Clark, E. L.; Bell, A. T. Direct Observation of the Local Reaction Environment during the Electrochemical Reduction of CO2. *J. Am. Chem. Soc.* **2018**, *140* (22), 7012−7020.
(45) Oda, I.; Ogasawara, H.; Ito, M. Carbon Monoxide Adsorption on Copper and Silver Electrodes during Carbon Dioxide Electroreduction Studied by Infrared Reflection Absorption Spectroscopy and Surface-Enhanced Raman Spectroscopy. *Langmuir* **1996**, *12*, 1094−1097.
(46) Firet, N. J.; Smith, W. A. Probing the Reaction Mechanism of CO2 Electroreduction over Ag Films via Operando Infrared Spectroscopy. *ACS Catal.* **2017**, *7*, 606−612.
(47) Peterson, A.; Nørskov, J. Activity Descriptors for CO2 Electroreduction to Methane on Transition Metal Catalysts. *J. Phys. Chem. Lett.* **2012**, *3*, 251−258.
(48) Hansen, H. A.; Varley, J. B.; Peterson, A. A.; Nørskov, J. K. Understanding Trends in the Electrocatalytic Activity of Metals and Enzymes for CO2 Reduction to CO. *J. Phys. Chem. Lett.* **2013**, *4*, 388−392.
(49) Nørskov, J. K.; Rossmeisl, J.; Logadottir, A.; Lindqvist, L.; Kitchin, J. R.; Bligaard, T.; Jónsson, H. Origin of the Overpotential for Oxygen Reduction at a Fuel-Cell Cathode. *J. Phys. Chem. B* **2004**, *108*, 17886−17892.
(50) Singh, M. R.; Goodpaster, J. D.; Weber, A. Z.; Head-Gordon, M.; Bell, A. T. Mechanistic Insights into Electrochemical Reduction of CO2 over Ag Using Density Functional Theory and Transport Models. *Proc. Natl. Acad. Sci. U. S. A.* **2017**, *114*, E8812−E8821.
(51) Wuttig, A.; Yaguchi, M.; Motobayashi, K.; Osawa, M.; Surendranath, Y. Inhibited Proton Transfer Enhances Au-Catalyzed CO2-to-Fuels Selectivity. *Proc. Natl. Acad. Sci. U. S. A.* **2016**, *113*, E4585−E4593.
(52) Dunwell, M.; Yang, X.; Setzler, B. P.; Anibal, J.; Yan, Y.; Xu, B. Examination of Near-Electrode Concentration Gradients and Kinetic Impacts on the Electrochemical Reduction of CO2 Using Surface-Enhanced Infrared Spectroscopy. *ACS Catal.* **2018**, *8*, 3999−4008.
(53) Nørskov, J. K.; Bligaard, T.; Logadottir, A.; Kitchin, J. R.; Chen, J. G.; Pandelov, S.; Stimming, U. Trends in the Exchange Current for Hydrogen Evolution. *J. Electrochem. Soc.* **2005**, *152*, J23−J26.
(54) Chen, L. D.; Urushihara, M.; Chan, K.; Nørskov, J. K. Electric Field Effects in Electrochemical CO2 Reduction. *ACS Catal.* **2016**, *6*, 7133−7139.
(55) Chan, K.; Eikerling, M. A Pore-Scale Model of Oxygen Reduction in Ionomer-Free Catalyst Layers of PEFCs. *J. Electrochem. Soc.* **2011**, *158*, B18−B28.
(56) Hamelin, A.; Vitanov, T.; Sevastyanov, E.; Popov, A. The Electrochemical Double Layer on Sp Metal Single Crystals: The Current Status of Data. *J. Electroanal. Chem. Interfacial Electrochem.* **1983**, *145*, 225−264.
(57) Fumagalli, L.; Esfandiar, A.; Fabregas, R.; Hu, S.; Ares, P.; Janardanan, A.; Yang, Q.; Radha, B.; Taniguchi, T.; Watanabe, K.; Gomila, G.; Novoselov, K. S.; Geim, A. K. Anomalously Low Dielectric Constant of Confined Water. *Science (Washington, DC, U. S.)* **2018**, *360* (6395), 1339−1342.
(58) Chelvayohan, M.; Mee, C. H. B. Work Function Measurements on (110), (100) and (111) Surfaces of Silver. *J. Phys. C: Solid State Phys.* **1982**, *15* (10), 2305−2312.
(59) Bachetta, M.; Trasatti, S.; Doubova, L.; Hamelin, A. The Dependence of the Potential of Zero Charge of Silver Electrodes on the Crystallographic Orientation of the Surface. *J. Electroanal. Chem. Interfacial Electrochem.* **1986**, *200*, 389−396.
(60) Hamelin, A.; Stoicoviciu, L.; Doubova, L.; Trasatti, S. Influence of the Crystallographic Orientation of the Surface on the Potential of Zero Charge of Silver Electrodes. *Surf. Sci.* **1988**, *201*, 498−506.
(61) Hori, Y.; Takahashi, I.; Koga, O.; Hoshi, N. Selective Formation of C2 Compounds from Electrochemical Reduction of CO2 at a Series of Copper Single Crystal Electrodes. *J. Phys. Chem. B* **2002**, *106*, 15−17.
(62) Mezzavilla, S.; Horch, S.; Stephens, I. E. L.; Seger, B.; Chorkendorff, I. Structure Sensitivity in the Electrocatalytic Reduction of CO_2 with Gold Catalysts. *Angew. Chem., Int. Ed.* **2019**, DOI: 10.1002/anie.201811422.
(63) Liu, M.; Pang, Y.; Zhang, B.; De Luna, P.; Voznyy, O.; Xu, J.; Zheng, X.; Dinh, C. T.; Fan, F.; Cao, C.; de Arquer, F. P. G.; Safaei, T. S.; Mepham, A.; Klinkova, A.; Kumacheva, E.; Filleter, T.; Sinton, D.; Kelley, S. O.; Sargent, E. H. Enhanced Electrocatalytic CO2 Reduction via Field-Induced Reagent Concentration. *Nature* **2016**, *537*, 382−386.

DOI: 10.1021/acscatal.9b00260
ACS Catal. 2019, 9, 4006−4014